ADVANCED MATERIALS TECHNOLOGIES
www.advmattechnol.de

Graded Kirigami Composites for Programmed Strain Distributions

*A B M Tahidul Haque, Dohgyu Hwang, and Michael D. Bartlett**

Stretchable devices and components have emerged as a vital platform for wearable electronics, biomedical sensors, and soft robotics. However, the soft-rigid interfaces that arise when integrating rigid components with soft and deformable substrates can cause stress concentrations, leading to premature failure of devices at these multi-material interfaces. Here, a stiffness-graded kirigami composite is introduced to control strain transitions at soft-rigid interfaces. The graded composite consists of soft elastomers bonded to rigid kirigami films with defined beam architectures to tune the stiffness gradient along the loading direction. Kirigami geometry is designed by coupling finite element analysis with experimental digital image correlation to achieve diverse strain profiles for flexible interfaces. Furthermore, an inverse design method is utilized to determine kirigami patterns to obtain predefined strain fields. These stiffness-graded kirigami composites create opportunities for more robust soft-rigid interfaces and defect-tolerant stretchable devices and robots.

1. Introduction

Stretchable and soft electronics are critical components for emerging technologies ranging from wearable electronics[1–4] and biomedical devices[5–7] to energy harvesting[8–10] and soft robotics.[11–14] These devices should be capable of bending, twisting, and stretching while they are integrated with various high-performance electronic components.[15–18] These multi-material systems often consist of rigid batteries, diodes, capacitors, processors, and wires.[19–23] Due to the compliance mismatch between the rigid and soft components, the strain in the stretched device changes rapidly at the soft–rigid interface.[24] This can accelerate localized rupture and lead to mechanical failure and electronic malfunction. Furthermore, rigid electronics often have low fracture strain (≤1%) and high elastic modulus (≫1GPA),[25–27] which must be considered during the design of stretchable devices. One approach to create stretchable devices is to incorporate rigid components onto strain isolated zones in a soft substrate.[17,24,28] For example, by modulating thickness across a soft substrate, the system localizes deformations in thinner regions while protecting electronics placed on thicker regions.[28–30] Similarly, strain isolation can be achieved by embedding or bonding rigid materials to limit strain.[17,24] However, these strain isolation approaches can still lead to large jumps in strain as the transition between the two regions is sharp at the interface.

Another approach to create robust stretchable electronics is to incorporate mechanically graded materials into soft substrates.[17,31] The gradient aims to smooth the rigidity mismatch by relieving the sharp stress concentration within the deformed substrate. For example, the gradient can be enabled by printing with different compositions of multiple constituents across a sheet,[31] diffusing uncured polymers radially at prescribed locations,[25] or solvent-welding layers of cured polymers with different levels of rigidity.[29] These methods often require precise control of chemical composition to induce gradients which can increase manufacturing complexity. Recent advances in mechanical metamaterials, which achieve advanced properties through material structure instead of composition, have enabled systematic controlling of engineering properties.[32–35] For example, a sheet with a layout of cut patterns, also known as kirigami, shows high stretchability[36–39] and shape transformation[40–42] on 2D sheets without changing compositions. The unique shape reconfiguration ability of kirigami architecture has been realized in wearable thermo-therapeutic devices,[43] electronic skin applications,[44] and strain sensors.[45] By creating gradients of geometric parameters in a kirigami sheet, the rigidity becomes graded which results in complex, heterogeneous strains under loading.[46–50] Such approaches could also provide benefits to program strain distributions in 2D sheets; however, the evolution of local strains across a multilayer kirigami sheet remains underexplored.

Here, we introduce a bi-layer kirigami composite with graded geometry that enables programmed strain distributions across a stretchable sheet. The composite consists of a kirigami sheet bonded to a continuous, soft elastomeric membrane, where the kirigami geometry is varied across the sheet to control strain gradients. This multilayered geometry generates various global strain gradients and can be programmed to control strain fields

A. B. M. T. Haque, D. Hwang, M. D. Bartlett
Mechanical Engineering
Soft Materials and Structures Lab
Virginia Tech
Blacksburg, VA 24060, USA
E-mail: mbartlett@vt.edu
D. Hwang, M. D. Bartlett
Macromolecules Innovation Institute
Virginia Tech
Blacksburg, VA 24060, USA

The ORCID identification number(s) for the author(s) of this article can be found under https://doi.org/10.1002/admt.202101241.

DOI: 10.1002/admt.202101241

 © 2021 Wiley-VCH GmbH

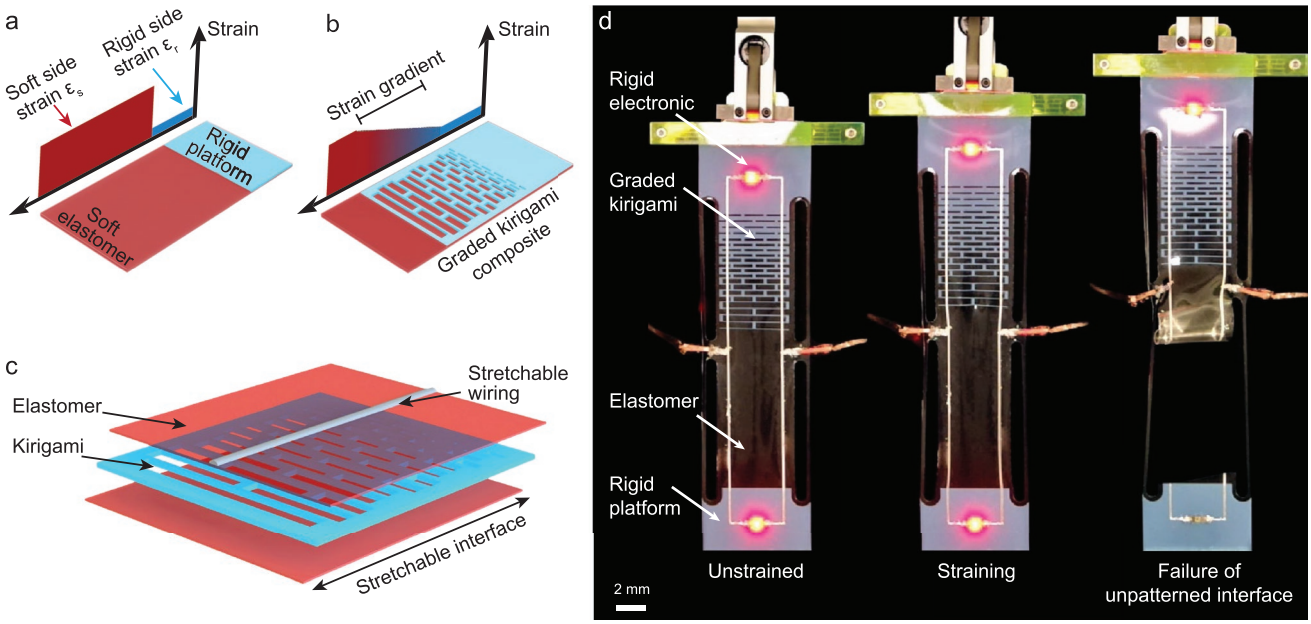

Figure 1. Graded kirigami patterns for soft–rigid interfaces. a) Unpatterned and b) graded kirigami embedded stretchable interface. c) Schematic of a multilayered composite showing the kirigami layer is encapsulated by elastomer. d) Stretchable electronics demonstration illustrates that a graded-kirigmai soft–rigid interface outlasts an unpatterned interface when loaded in series.

in distinct sub-regions across the sheet. In contrast to previous studies which may embed a single rigid layer of material or create chemical gradients to tune local modulus, kirigami can be utilized in a range of materials and displays a versatile design space by modifying beam geometry, spacing, and arrangement to create prescribed strain profiles. Graded kirigami composites are also capable of globally distributing strain across a planar sheet. Here, we create and evaluate kirigami designs by combining experimental and numerical methodologies, where a computational parametric study is guided with experimental digital image correlation (DIC) studies. Strain gradient metrics are introduced and strain transitions are created at soft-rigid interface through an inverse design methodology. We develop various linear and nonlinear strain maps and program the kirigami grading to obtain the target profiles. This inverse design methodology offers the ability to create diverse strain profiles, which we demonstrate with both smooth and step-wise strain gradients across a sheet. This graded-kirigami methodology provides a mechanism to engineer strain gradients in deformable substrates by incorporating a continuous, patterned sheet with no discrete elements. The continuous nature of the patterned kirigami film can also simplify handling and assembly compared to discretized materials, as the kirigami films can be placed onto a substrate as a single sheet. This enables an approach to bond kirigami graded skins onto soft substrates to control strain gradients for more robust soft–rigid interfaces for emerging soft technologies.

2. Results and Discussion

2.1. Methodology of Kirigami Patterning

The multilayered composites are created by embedding a stiff polymer film of polyethylene terephthalate (PET) (modulus ≈ 1.9 GPa) inside a polydimethylsiloxane (PDMS) silicone elastomer (modulus ≈ 2 MPa). Since PET is nearly 1000 times stiffer than PDMS, it experiences negligible deformation and creates a strain isolation zone for electronics incorporation. In contrast, the soft PDMS can significantly deform to carry almost all of the applied stretch. **Figure 1**a shows the layout of a conventional rigid–soft interface where a PET sheet is embedded inside a soft elastomer. The compliance mismatch between the two distinct regions causes a large difference in strains at the soft (ε_s) and rigid (ε_r) region, respectively, which can lead to a premature mechanical failure at the interface. To overcome the sharp interface, we place a graded kirigami composite between the incompatible rigid and soft regions (Figure 1b). This graded kirigami functions as a stretchable interface which enables gradient strain profile to gradually change the strain from ε_s to ε_r. Figure 1c shows a multilayered stretchable interface where the soft elastomers encapsulate a PET sheet with graded kirigami beam architectures. The kirigami consists of spatially varying unit cells to tune the stretchable interface stiffness from the soft to rigid edges. Here, the PET layer is fabricated with a CO_2 laser which allows us to create beams with dimensions down to 0.5 mm. The graded kirigami approach should also be suitable for sub-millimeter and sub-micron applications. With microscale fabrication techniques such as photolithography,[36] focused ion beam milling,[51] and laser micromachining,[52] kirigami properties can be scaled to smaller length scales. The utility of kirigami-gradients are demonstrated in Figure 1d where two rigid electronic components (LEDs) are placed on an unpatterned and kirigami patterned interface. The LEDs are connected in parallel electrically while the platforms are mechanically in series. Upon stretching, the graded kirigami interface survives while the traditional soft-rigid interface suffers an early failure.

© 2021 Wiley-VCH GmbH

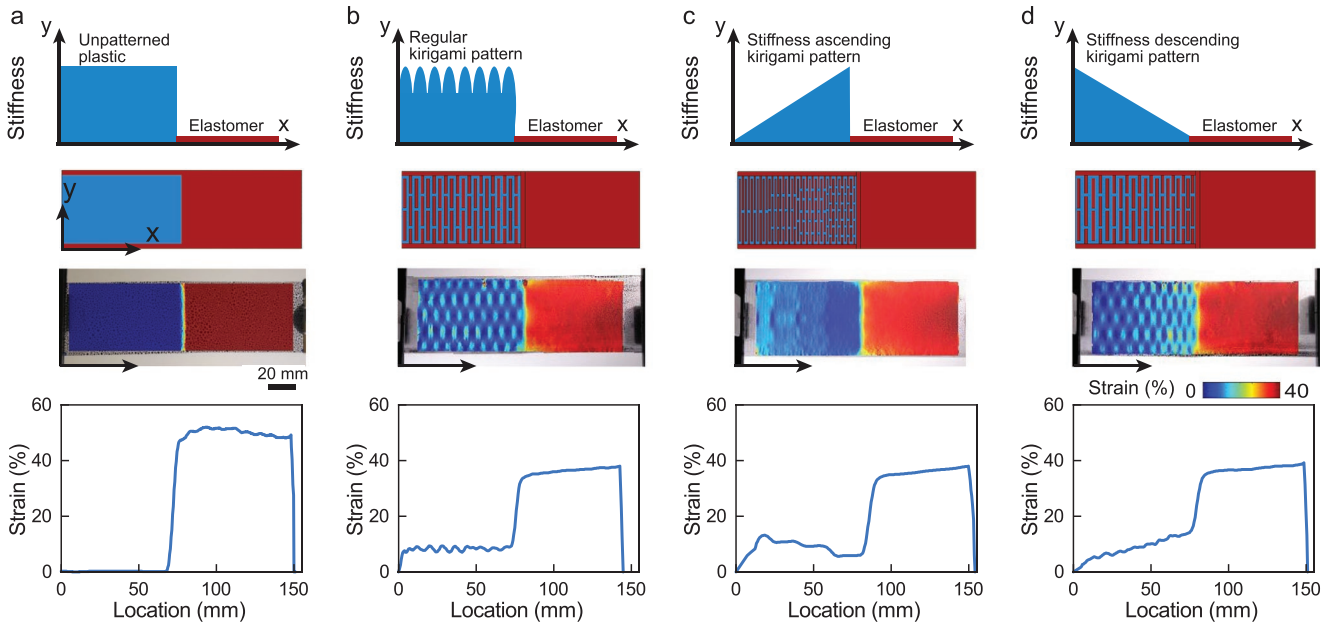

Figure 2. Graded kirigami to mitigate compliance mismatch at interfaces. a) Traditional rigid platform, b) uniform kirigami embedded composite, c) ascending graded stiffness of a kirigami composite, and d) descending graded stiffness of a kirigami composite. The rows from top represent a stiffness schematic, representative composite design, strain contour map from DIC, and the strain profile across the interface. A global strain of 25% is applied for all the designs.

The kirigami patterns are designed by a performance driven study consisting of experimental and computational analyses. The strain field during stretching is experimentally measured using DIC and the computational analysis is performed using finite element (FE) analysis. Previous studies have used DIC,[25,28] FEA,[26,28,29] and their combination[27,30] [53] to determine metamaterial deformations. Here, we integrate DIC and FE in a feedback-control scheme for the strain gradient performance. **Figure 2** shows that the composites are in the $x - y$ plane where strain is applied along the x-axis for different configurations of the soft–rigid interfaces. We conduct the DIC and FE analysis for planar deformation field in the $x - y$ plane where the compliance mismatch should be mitigated. The first row of Figure 2 gives a qualitative representation of stiffness along the x-axis and the second row provides schematics of the composite design. The DIC strain maps and corresponding strain profiles of the four soft–rigid interfaces are presented for 25% global stretching in the third and fourth row, respectively. Figure 2a shows a conventional rigid platform without any structural pattern where we observe an abrupt strain change across the interface. In addition, the strain profile along the composite length (i.e., x-axis) indicates that strain is nearly zero for the PET region with a step change to almost 50% at the elastomer zone. Next, we pattern kirigami openings to impart stretchability in the PET and bond this film to a continuous elastomer layer. The addition of kirigami is useful to change the stiffness of the transition zone; however, Figure 2b shows that a uniform pattern is not sufficient to mitigate the soft–rigid interface issue. We still observe a sudden change of strain in the strain profile of Figure 2b alongside some deformation spikes at kirigami openings. Instead of periodic kirigami cuts, combinations of kirigami patterns are needed to gradually change the strain of the transition zone to make it a stretchable interface. Figure 2c shows an ascending stiffness kirigami configuration where stiffness increases toward the elastomer. This is not ideal, as this introduces a soft–rigid compliance mismatch at the beginning and end of kirigami. A more desirable soft–rigid interface should show descending stiffness from the rigid to soft interface. We create a gradient where strain increases from nearly zero to a value which is approaching the strain in the soft elastomer. This provides a smoother transition from the rigid to soft components (Figure 2d). This structure contains six graded kirigami regions with variable geometric parameters within each region. Furthermore, a strain profile comparison of Figures 2a and 2d shows that the addition of kirigami reduces the local elastomer strain for equal global stretching. These results demonstrate that kirigami composites can generate different strain profiles across a sheet by tuning kirigami geometry. We also performed a cyclic tensile test on a graded kirigami composite for 25 cycles (Figure S1, Supporting Information). After the first cycle, small hysteresis appeared in subsequent cycles. We also observed a minor softening effect after the initial cycle. These effects are similar to the Mullins effect seen in other soft composite materials. Due to the similar behavior over multiple cycles, the kirigami composite can be repetitively used.

2.2. Parametric Analysis for Graded Patterns

The experimental observations from DIC analysis provide valuable insight into the effect of kirigami structure on strain gradient profile. Notice that the improved strain profile in Figure 2d still contains a strain jump at soft–rigid interface. To obtain a smoother strain gradient, we utilize finite element analysis (FEA) as an efficient platform to simulate kirigami patterns. This enables us to conduct a parametric study more rapidly than with experiments alone

© 2021 Wiley-VCH GmbH

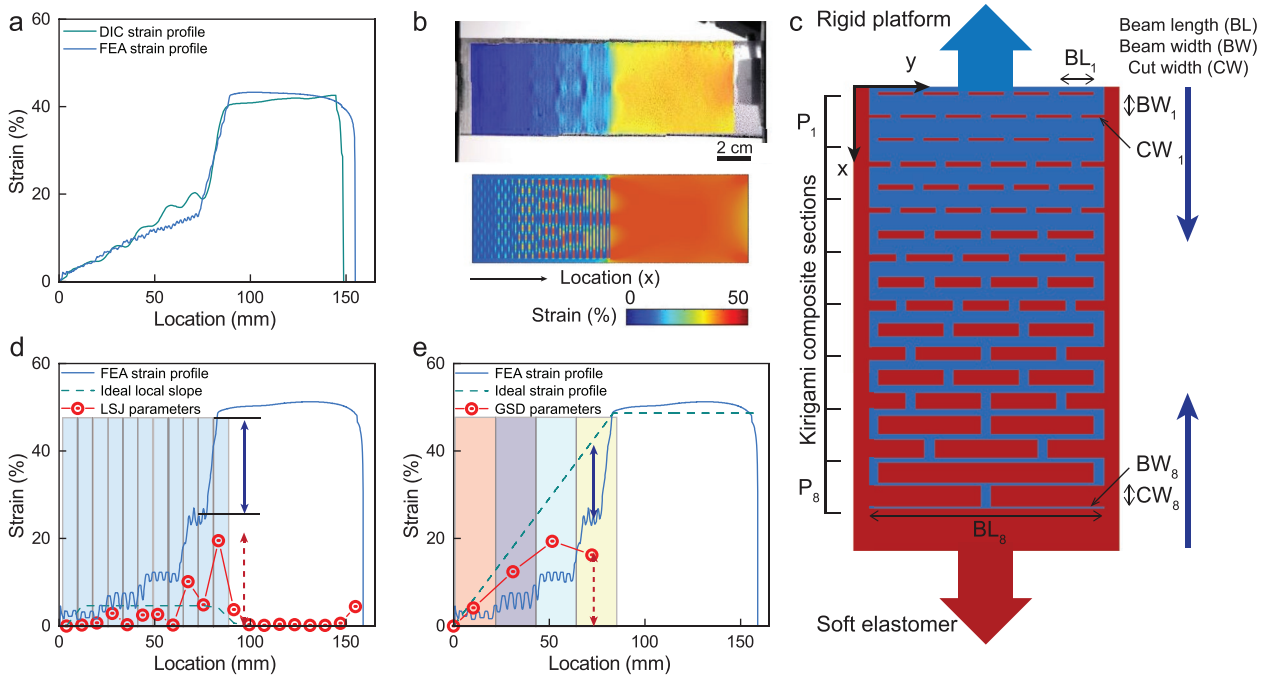

Figure 3. Model development and performance indicators for parametric strain studies. Comparison of DIC analysis and FE analysis using a) strain profile and b) strain map for 30% global strain to validate the computational model. c) Geometric parameters for the parametric studies distributed into eight sections. The arrows on the right side show the direction of increasing length for the respective parameter. Calculation procedure of performance indicators from ideal and measured strain profiles for d) local strain jump (LSJ) and e) global strain deviations (GSD) in a FEA strain profile.

to evaluate the effect of kirigami design parameters such as size of unit cells, beam layer configurations, and sequences of patterns. Therefore, we investigate the strain profile of kirigami patterned structures using nonlinear FEA program ABAQUS. To develop a computational model, we mechanically characterize the composite material and elastomeric substrate. The constitutive stress–strain relation obtained from the experiments are incorporated into the FE simulation using elastic and hyperelastic material models. Similar to the experimental stretching procedure, the elastomer edge of the sheet in simulations is fixed and a deformation boundary condition is created at the kirigami composite side to prescribe a strain. We use a 3D platform for the FE model to allow both in-plane and out-of-plane deformations. Next, we create several kirigami models in FEA and compare the numerical simulation results with the strain profile from the experimental DIC analysis. Multiple element sets are defined along the longitudinal direction x so that the average strain across the width (y-axis) can be determined in a similar manner to the experimental results. Note that, due to the focus on planar deformation, we extract in-plane strain fields for both DIC and FE analysis. **Figure 3**a,b shows a comparative strain profile which validates the model with good agreement of DIC and FE results. The validated numerical model is incorporated in a set of computational scripts to parameterize the critical geometric variables of the kirigami composite. A representative composite schematic with the variable features is shown in Figure 3c. Here, the kirigami film and elastomer are represented by blue and red areas, respectively. The system is 52 mm wide and both the kirigami and elastomer zones are nearly 80 mm long. Along the transverse direction (y-axis), we maintain a constant spacing of 2 mm between consecutive beams and use edge encapsulation of 3 mm. The kirigami is partitioned into eight small segments (10 mm each) along the length which are denoted by P_N for N-th pattern. In each kirigami section, we explore the beam width BW_N, cut width CW_N (i.e., kirigami opening), and beam length across the kirigami width BL_N (i.e., number of beams in transverse direction).

To efficiently design the stretchable interface at the soft–rigid interface, we identify two strain gradient performance indicators: the local strain jump (LSJ) and global strain deviations (GSD). Local strain jump (LSJ) in Figure 3d refers to strain spikes inside the kirigami caused by inadequate stiffness tuning along the specimen length. We monitor this disruption by dividing the stretchable interface into 11 sections (8 mm each) and find the average strain in each section. Specifically, 10 sections are inside the kirigami region with an additional section at the end to find the strain jump between the stretchable interface and the elastomer. Then, the LSJ parameter of a section is calculated by taking the difference in average strain between the current section and the preceding section. LSJ can be viewed as a slope of strain along the length, where a liner increase in strain along the length would have a constant LSJ value, as indicated by the green dotted line in Figure 3d. A large LSJ can indicate a potential failure region where a larger than desired strain jump is present. Even if a kirigami grading reaches the desired strains at the beginning and end, the stretchable platform could still suffer from strain spikes in the middle. The global strain deviation (GSD) refers to the departure of the actual strain profile from the ideal interface strain. Here, we consider a linear strain profile to connect the soft and rigid edges which is shown by the dotted line in Figure 3e. For a stretched kirigami composite, the average strain is measured for each quarter segment represented by four shaded region

© 2021 Wiley-VCH GmbH

of the stretchable interface in Figure 3e. Then, four GSD parameters are determined from the difference of the target and actual kirigami strains of the respective quarter. This global deviation is an indicator of compliance mismatch at the soft–rigid interface. Even if a kirigami grading appears to achieve a linear strain profile, it could still fall short of the elastomer strain at the end of stretchable interface as seen in Figure 3a. The GSD parameters detect this mismatch across the interface and a set of small GSD values signifies an acceptable graded kirigami pattern. The combination of LSJ and GSD can evaluate the strain disruptions corresponding to local and global compliance mismatch, respectively.

2.3. Performance-Driven Graded Kirigami Design

To determine the effect of different geometric parameters on the kirigmi composite stiffness, we develop separate computational models with periodic (i.e., not spatially varied) patterns. A global strain of 30% is applied to all the parametric models of this study. Figure S2a, Supporting Information, shows a unique kirigami with a periodic unit cell which could fill a section in a graded kirigami. The stiffness for a unique pattern can be determined from the simulated force–displacement relation presented in Figure S2b, Supporting Information. To identify the mechanical influence of a parameter such as beam length BL, we explore a set of unique kirigami designs each with different BL, but same cut width CW and beam width BW. Figure S3a, Supporting Information, represents the stiffness of the unique kirigami models as a function of BL. Similarly, Figures S3b and S3c show the specific influences of CW and BW, respectively. We find that stiffness of kirigami models decreases with increase of BL and CW and decrease of BW. Recall that we need a descending stiffness trend from rigid to soft side. So, Figure 2c explains the required trend of increasing

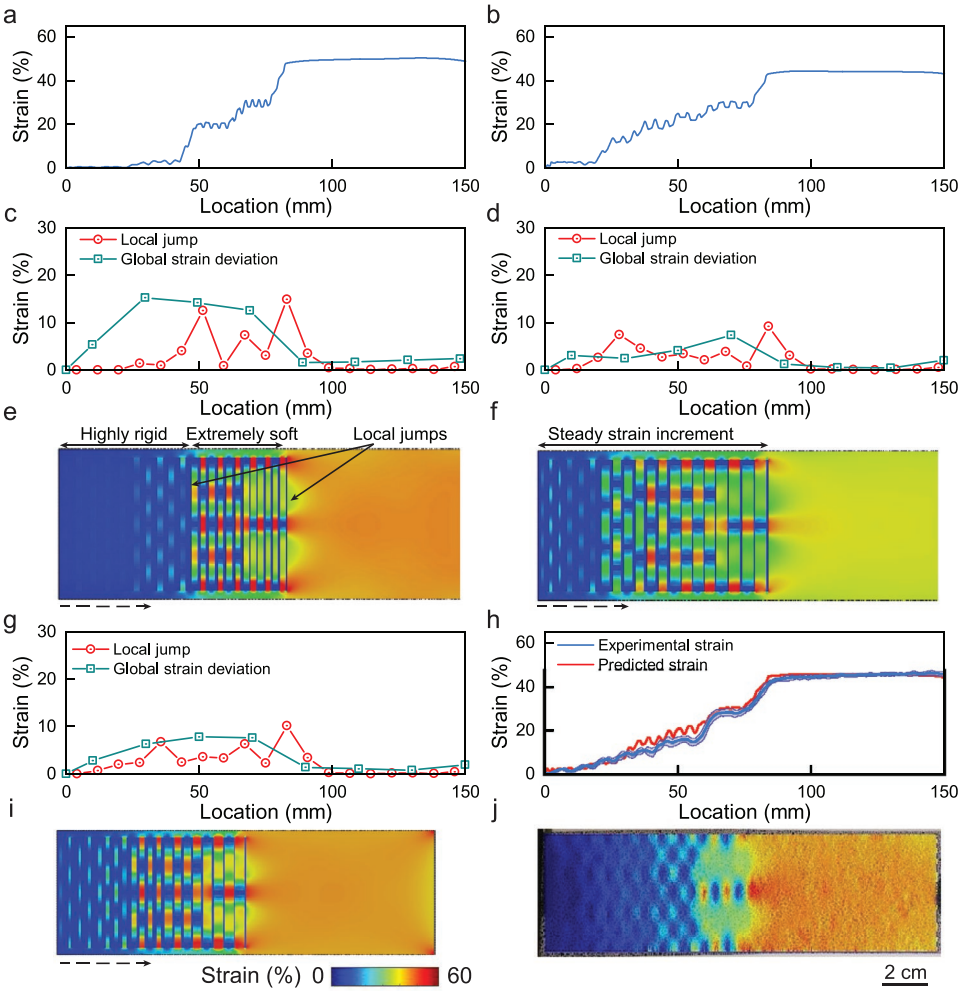

Figure 4. Design of graded kirigami composite for stretchable soft–rigid interface. Sample strain profiles of a) initial and b) improved kirigami grading. c) High values of LSJ and GSD indicate inadequate design of initial model. d) Low LSJ and GSD represent better performance of improved model. e) The strain contour of the initial model shows inadequate grading and corresponding local strain jumps. f) The contour map of improved grading shows a more gradual strain increment. g) LSJ and GSD results of a high-performing kirigami grading which is selected for experimental evaluation. h) Parametric study is validated by comparison of simulation strain with the average strain profiles from multiple experiments. The shaded area represents standard deviation of different experimental specimen. i) Strain field from the FEA and j) DIC for the high-performing kirigami grading. A 30% global strain is applied for all the plots and a local strain scale of 0–60% is used for all the contour plots.

© 2021 Wiley-VCH GmbH

BL and CW and decreasing BW dimensions as we approach from segment 1 to 8.

We use these different kirigami designs to arrange patterns for the graded kirigami composites. The parametric study encompassing various geometric features and pattern layouts are evaluated through performance indicators LSJ and GSD. Figure S4a, Supporting Information, shows the collection of maximum LSJ and average GSD for all the computational models analyzed for this parametric study. Representative initial and improved strain profiles are shown in **Figures 4**a and 4b, respectively. The performance indicators in Figure 4c show the initial design displays large values (>10%) of LSJ and GSD. Figure 4d presents an improved kirigami grading that show that shows significantly smaller (<10%) performance indicators. The strain contour maps of the initial and improved models are shown in Figures 4e and 4f, respectively. Figure 4e shows rapid change of strain due to compliance mismatch between rigid and soft patterns. High LSJs at the locations of 50 and 80 mm in Figure 4c directly correspond to the local strain jump indicated in Figure 4e. The highly rigid kirigami patterns between 0–40 mm are also the cause of high GSD values in that area. On the other hand, a steady strain increase is shown in Figure 4f by a balanced compliance grading of kirigami patterns.

We have selected one high-performing computational model to examine the prediction accuracy of our parametric study. This graded kirigami is characterized by small LSJ and GSD values as shown in Figure 4g. We fabricated an experimental sample of the model and performed DIC analysis for tensile loading. Figure 4h shows that the experimental strain profile coincides with the simulation results. We present the strain map from FE simulation in Figure 4i and DIC analysis in Figure 4j to show the gradual strain distribution across the stretchable interface. We note that the strain gradients of the composite are governed by the geometric patterning of kirigami. We have conducted a set of FE analyses where the elastomer thickness is increased by factors of 1.2×, 1.5×, and 2.0× relative to the initial elastomer thickness. Figure S7, Supporting Information, shows that despite the addition of elastomer thickness, the strain gradient profiles are maintained.

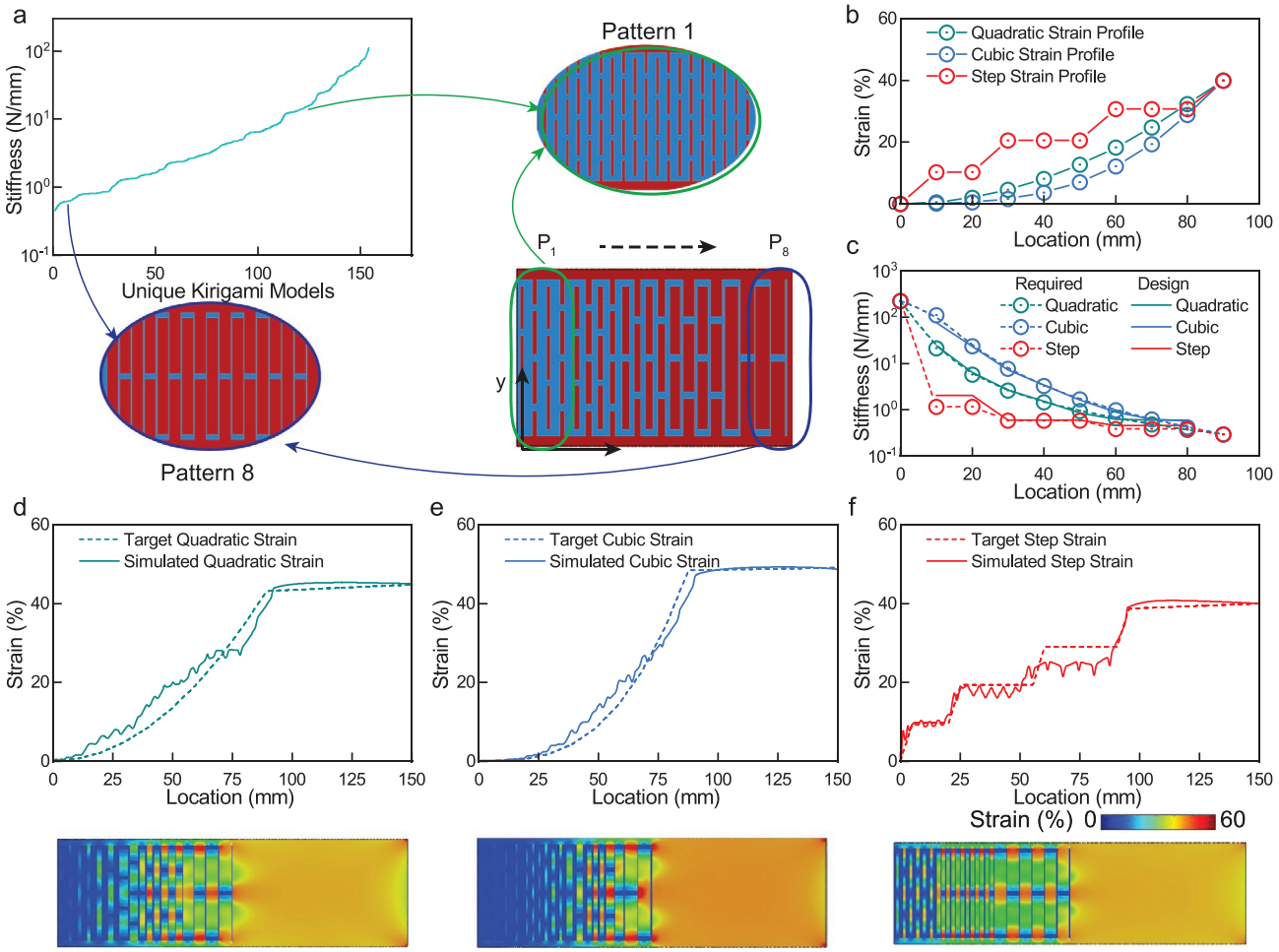

Figure 5. Inverse design of kirigami composites for target strain profiles. a) Plot of stiffness for unique kirigami models shows the stiffness range available for inverse design. Schematic showing the kirigami grading starting with a rigid model at section 1 and finishing with a low stiffness kirigami model near the elastomer. b) Target polynomial and step strain profiles for inverse design. c) Circle marked dotted lines show the stiffness required at different sections to reach the target strain. The solid lines present the graded stiffness of kirigami compiled by sequencing unique models. Target and simulated strain results for d) quadratic, e) cubic, and f) step strain profiles. The corresponding strain contour from FE analysis are shown under each profile. A 30% global strain is applied for all the plots and a local strain scale of 0–60% is used for all the contour plots.

 © 2021 Wiley-VCH GmbH

2.4. Predictive Kirigami Design for Target Strain Profiles

The relationship between stiffness and strain controls the deformation profiles in the kirigami composite. For a target strain profile, the required stiffness can be obtained by considering linear elastic deformations in the kirigami segments. The average segment strain ε_s (s = segment) is used to determine the stiffness of that segment by $k_s = F/(L_s\varepsilon_s)$, where F and L_s are unit force and segment length, respectively. This provides a methodology to determine the required stiffness values along the length of the sample to create different strain profiles. Through the parametric study on homogenous kirigami designs, we compiled a kirigami library in **Figure 5**a, which shows a stiffness range of 0.45–111.4 N mm^{-1}. This library can be used to create various strain profiles for the stretchable interface by selectively placing kirigami patterns at different locations (as shown by the schematic process in Figure 5a).

Strain profiles beyond the linear gradient of Figure 4 could also be achieved using different arrangements of kirigami. To show the adaptability of the predictive modeling, we consider higher order polynomial curvatures and step strain profiles as shown in Figure 5b. Our objective is to connect the rigid platform strain ε_r and elastomer strain ε_e by 2 and 3 degree polynomials and a 3 stepped ramp strain profile. By keeping ε_r and ε_e, respectively, as start and end strain, we can set up the required strain along kirigami segments for a target profile. Figure 5c shows the stiffness required (dotted line) and the available kirigami designs (solid line) at different segments for the quadratic, cubic, and step strain profiles (detailed calculation can be found in the Supporting Information).

In order to design distinct kirigami grading for different stiffness profiles, we perform nearest-neighbor search in the stiffness library of Figure 5a and then selectively place this kirigami geometry in the graded kirigami design. Figures 5d,e, and 5f show the target and simulated strains across the stretchable platform for quadratic, cubic, and step profiles, respectively. We find good agreement between these profiles showing the ability to create diverse strain gradients across stretchable substrates.

3. Conclusion

We have developed a kirigami programming technique to design graded stiffness profiles for strain engineering. The spatial pattering of geometric features makes kirigami a robust approach to control compliance mismatch in stretchable devices. By varying the kirigami layout, we created a group of unique kirigami patterns where the stiffness spans 0.45–111.4 N mm^{-1} to cover a stiffness range >200×, enabling the creation of different strain gradients under uni-axial loading. This can provide a tool to tune stiffness across a sheet without changing chemical composition. The stiffness grading could also be adopted for biaxial kirigami cuts which could enhance multiaxial stretchability. As the properties are controlled by the structure, we anticipate this approach can also be applied to diverse materials and is suitable for rapid manufacturing of the graded composites. Through an FEA-based computational framework coupled with DIC, we utilized performance-based strain metrics to create diverse kirigami arrangements to control strain transitions at soft–rigid interfaces. The stiffness tunability is expanded in our inverse modeling method by utilizing the compliance–deformation relations of kirigami sub-structures to sequence their pattern. By bonding kirigami graded sheets onto soft substrates, we can control strain gradients at soft–rigid interfaces for emerging soft technologies. For example, this could include biomedical sensors where gradients could improve interfacing of rigid components to skin during health monitoring. In soft robotics, the sheets could smooth strain gradients between external connections or embedded rigid sensors with the soft, deformable body, or could also be implemented into pneumatic actuators for controlling deformation during locomotion or gripping. There could also be utility in reconfigurable structures to control strain distributions during deployment. Therefore, we anticipate that the programmable strain approach of the stiffness-graded kirigami composites can have impact in fields of stretchable electronics, robotic actuators, reconfigurable structures, and flexible sensors.

4. Experimental Section

Kirigami Composite Fabrication: Kirigami composites were composed of a stiffness tuning layer and encapsulating elastomers. A thin PDMS elastomer (Sylgard 184 with a 10:1 base-to-curing ratio, $t \approx = 250$ µm, Dow Corning) was created on a glass plate using a thin-film applicator (ZUA 2000, Zehntner Testing Instruments) and cured at 80 °C for 1 h. A PET film ($t = 125$ µm, Grainger) was patterned using a laser cutter (Epilog Laser Fusion M2, 75 w) to create the stiffness tuning layer and treated with oxygen plasma (pressure : 300 mTorr, 3 min, Plasma Etch). Another batch of PDMS of an identical mixing ratio was cast onto the cured PDMS layer using a thin film applicator ($t = 30$ µm), and the treated PET film was brought into contact with the precured layer. A final batch of PDMS of an identical mixing ratio was cast onto the deposited film and cured at 80 °C for 1 h to create an encapsulated composite.

Mechanical Testing: Specimens (PDMS with a 10:1 base-to-curing ratio and PET) were prepared in a dogbone shape, and tensile testing was performed on an Instron 5944 mechanical testing machine at a displacement rate of 1 mm s^{-1}.

DIC: The DIC program Ncorr was used, which is formulated using a subset-based DIC algorithm. The program is capable of correlating high-strain fields by continuously updating the reference images during stretching. In order to calculate the strain field of composites, the DIC program requires a group of discernible features on the specimen. Therefore, black spackles were created on the composite surface using ink spray (Speedball Super Black India Ink) which could be marked by the program to track the elongation during tensile test. The tensile deformation of kirigami composites were recorded using a high-resolution digital camera (Pentax K-1 Mark II) and images at 1 s interval were collected using MATLAB Image Processing Toolbox. The post processing of the DIC results were performed using the program Ncorr_post to obtain strain values throughout a line crossing the soft-rigid platform. The uniaxial strain profile was determined for the stretching direction x (see Figure 2) by taking the average values of full width along y. This resulted in longitudinal strain profiles presenting the average strain in the transverse direction of a composite.

FEA: The FE analysis of graded kirigami composite was conducted in ABAQUS program (SIMULIA, Providence, RI). The homogeneous elastomer sections were simulated using Yeoh hyperelastic[54] model (more details in the Supporting Information). The 3D model was meshed using S4R elements which was a four-noded finite-strain shell formulated by reduced integration with hourglass control. These are 3D shell elements which do not restrict non-planar deformation. A small seed size of 1 mm was used to create the mesh with five integration points through thickness to achieve simulation convergence. In order to conduct parametric study of various geometric compositions, master script was formulated using Python. The

© 2021 Wiley-VCH GmbH

permutation was assembled using MATLAB to sequentially generate FE models from script and post process the simulation results.

Supporting Information

Supporting Information is available from the Wiley Online Library or from the author.

Acknowledgements

The authors acknowledge support through the Defense Advanced Research Projects Agency Young Faculty Award (DARPA YFA) (D18AP00041) and the Office of Naval Research Young Investigator Program (YIP) (N000142112699).

Conflict of Interest

The authors declare no conflict of interest.

Data Availability Statement

The data that support the findings of this study are available from the corresponding author upon reasonable request.

Keywords

finite element analysis, kirigami, soft-rigid interface, strain engineering, stretchable electronics

Received: September 20, 2021
Revised: November 5, 2021
Published online:

[1] O. A. Araromi, M. A. Graule, K. L. Dorsey, S. Castellanos, J. R. Foster, W.-h. Hsu, A. E. Passy, J. J. Vlassak, J. C. Weaver, C. J. Walsh, R. J. Wood, *Nature* **2020**, *587*, 219.
[2] J. Wang, H. Lou, J. Meng, Z. Peng, B. Wang, J. Wan, *Sensors & Actuators: B. Chemical* **2020**, *305*, 127529.
[3] E. J. Park, T. Akbas, A. Eckert-Erdheim, L. H. Sloot, R. W. Nuckols, D. Orzel, L. Schumm, T. D. Ellis, L. N. Awad, C. J. Walsh, *IEEE Transactions on Medical Robotics and Bionics* **2020**, *2*, 165.
[4] T.-G. La, S. Qiu, D. K. Scott, R. Bakhtiari, J. W. Kuziek, K. E. Mathewson, J. Rieger, H.-J. Chung, *Adv. Healthcare Mater.* **2018**, *7*, 1801033.
[5] D.-H. Kim, R. Ghaffari, N. Lu, J. A. Rogers, *Annu. Rev. Biomed. Eng.* **2012**, *14*, 113.
[6] M. A. Skylar-Scott, S. G. M. Uzel, L. L. Nam, J. H. Ahrens, R. L. Truby, S. Damaraju, J. A. Lewis, *Sci. Adv.* **2019**, *5*, eaaw2459.
[7] J. Deng, H. Yuk, J. Wu, C. E. Varela, X. Chen, E. T. Roche, C. F. Guo, X. Zhao, *Nat. Mater.* **2021**, *20*.
[8] E. Bortot, R. Denzer, A. Menzel, M. Gei, *Int. J. Solids Struct.* **2016**, *78-79*, 205.
[9] E. C. Warmann, P. Espinet-Gonzalez, N. Vaidya, S. Loke, A. Naqavi, T. Vinogradova, M. Kelzenberg, C. Leclerc, E. Gdoutos, S. Pellegrino, H. A. Atwater, *Acta Astronaut.* **2020**, *170*, 443.
[10] V. Vallem, Y. Sargolzaeiaval, M. Ozturk, Y.-C. Lai, M. D. Dickey, *Adv. Mater.* **2021**, *33*, 2004832.
[11] H. Bai, S. Li, J. Barreiros, Y. Tu, C. R. Pollock, R. F. Shepherd, *Science* **2020**, *370*, 848.
[12] K. Liu, F. Hacker, C. Daraio, *Sci. Rob.* **2021**, *6*, eabf5116.
[13] D. Zhalmuratova, H.-J. Chung, *ACS Applied Polymer Materials* **2020**, *2*, 1073.
[14] R. A. Bilodeau, A. M. Nasab, D. S. Shah, R. Kramer-Bottiglio, *Soft matter* **2020**, *16*, 5827.
[15] K.-B. Kim, Y.-J. Lee, A. Costa, Y.-K. Lee, T.-S. Jang, M.-G. Lee, Y.-C. Joo, K. H. Oh, J. Song, I.-S. Choi, *Adv. Eng. Mater.* **2019**, *21*, 1900206.
[16] J. W. Lee, R. Xu, S. Lee, K.-I. Jang, Y. Yang, A. Banks, K. J. Yu, J. Kim, S. Xu, S. Ma, S. W. Jang, P. Won, Y. Li, B. H. Kim, J. Y. Choe, S. Huh, Y. H. Kwon, Y. Huang, U. Paik, J. A. Rogers, *Proc. Natl. Acad. Sci. USA* **2016**, *113*, 6131.
[17] Y. Cao, G. Zhang, Y. Zhang, M. Yue, Y. Chen, S. Cai, T. Xie, X. Feng, *Adv. Funct. Mater.* **2018**, *28*, 1.
[18] A. T. Haque, R. Tutika, R. L. Byrum, M. D. Bartlett, *Adv. Funct. Mater.* **2020**, *30*, 2000832.
[19] R. Kumar, K. M. Johnson, N. X. Williams, V. Subramanian, *Adv. Energy Mater.* **2019**, *9*, 1803645.
[20] D. Wirthl, R. Pichler, M. Drack, G. Kettlguber, R. Moser, R. Gerstmayr, F. Hartmann, E. Bradt, R. Kaltseis, C. M. Siket, S. E. Schausberger, S. Hild, S. Bauer, M. Kaltenbrunner, *Sci. Adv.* **2017**, *3*, e1700053.
[21] X. Shi, S. Pei, F. Zhou, W. Ren, H.-M. Cheng, Z.-s. Wu, X. Bao, *Energy Environ. Sci.* **2019**, *12*, 1534.
[22] E. Markvicka, G. Wang, Y.-C. Lee, G. Laput, C. Majidi, L. Yao, in *Proc. of the 2019 CHI Conf. on Human Factors in Computing Systems*, ACM, New York **2019**, pp. 1–10. https://dl.acm.org/doi/10.1145/3290605.3300862.
[23] S. Lin, H. Yuk, T. Zhang, G. A. Parada, H. Koo, C. Yu, X. Zhao, *Adv. Mater.* **2016**, *28*, 4497.
[24] Z. Wu, S. Zhang, A. Vorobyev, K. Gamstedt, K. Wu, C. Guo, S. H. Jeong, *Materials Today Physics* **2018**, *4*, 28.
[25] N. Naserifar, P. R. LeDuc, G. K. Fedder, *J. Micromech. Microeng.* **2017**, *27*, 045018.
[26] I. M. Graz, D. P. J. Cotton, A. Robinson, S. P. Lacour, *Appl. Phys. Lett.* **2011**, *98*, 2009.
[27] A. Romeo, Q. Liu, Z. Suo, S. P. Lacour, *Appl. Phys. Lett.* **2013**, *102*, 98.
[28] Y. Lim, J. Yoon, J. Yun, D. Kim, S. Y. Hong, S.-J. Lee, G. Zi, J. S. Ha, *ACS Nano* **2014**, *8*, 11639.
[29] R. Libanori, R. M. Erb, A. Reiser, H. Le Ferrand, M. J. Süess, R. Spolenak, A. R. Studart, *Nat. Commun.* **2012**, *3*, 1.
[30] G. Cantarella, V. Costanza, A. Ferrero, R. Hopf, C. Vogt, M. Varga, L. Petti, N. Münzenrieder, L. Büthe, G. Salvatore, A. Claville, L. Bonanomi, A. Daus, S. Knobelspies, C. Daraio, G. Tröster, *Adv. Funct. Mater.* **2018**, *28*, 1.
[31] D. Kokkinis, F. Bouville, A. R. Studart, *Adv. Mater.* **2018**, *1705808*, 1.
[32] J. H. Pikul, S. Li, H. Bai, R. T. Hanlon, I. Cohen, R. F. Shepherd, *Science* **2017**, *358*, 210.
[33] Y. Tang, G. Lin, S. Yang, Y. K. Yi, R. D. Kamien, J. Yin, *Adv. Mater.* **2017**, *29*, 1604262.
[34] A. Rafsanjani, Y. Zhang, B. Liu, S. M. Rubinstein, K. Bertoldi, *Sci. Rob.* **2018**, *3*, 15.
[35] D.-G. Hwang, K. Trent, M. D. Bartlett, *ACS Appl. Mater. Interfaces* **2018**, *10*, 6747.
[36] M. K. Blees, A. W. Barnard, P. A. Rose, S. P. Roberts, K. L. McGill, P. Y. Huang, A. R. Ruyack, J. W. Kevek, B. Kobrin, D. A. Muller, P. L. McEuen, *Nature* **2015**, *524*, 204.
[37] M. Isobe, K. Okumura, *Sci. Rep.* **2016**, *6*, 24758.
[38] D.-G. Hwang, M. D. Bartlett, *Sci. Rep.* **2018**, *8*, 1.

© 2021 Wiley-VCH GmbH

[39] S. Charkhabi, Y. J. Chan, D.-G. Hwang, S. T. Frey, M. D. Bartlett, N. F. Reuel, *Adv. Mater. Technol.* **2019**, *4*, 1800683.
[40] A. Costa, V. Kunin, J.-H. Shin, I.-S. Choi, T. A. Kim, S. Yang, S. Y. Lee, J. Li, Y. Cho, D. J. Srolovitz, H. N. Han, *Proc. Natl. Acad. Sci. USA* **2014**, *111*, 17390.
[41] J. I. Azzopardi, A. Casha, J. N. Grima, D. Attard, J. Briffa, L. Mizzi, K. M. Azzopardi, R. Gatt, *Sci. Rep.* **2015**, *5*, 1.
[42] R. M. Neville, F. Scarpa, A. Pirrera, *Sci. Rep.* **2016**, *6*, 31067.
[43] N.-S. Jang, K.-H. Kim, S.-H. Ha, S.-H. Jung, H. M. Lee, J.-M. Kim, *ACS Appl. Mater. Interfaces* **2017**, *9*, 19612.
[44] P. Won, J. J. Park, T. Lee, I. Ha, S. Han, M. Choi, J. Lee, S. Hong, K.-J. Cho, S. H. Ko, *Nano Lett.* **2019**, *19*, 6087.
[45] K. Xu, Y. Lu, S. Honda, T. Arie, S. Akita, K. Takei, *J. Mater. Chem. C* **2019**, *7*, 9609.
[46] S. Shan, S. H. Kang, J. R. Raney, P. Wang, L. Fang, F. Candido, J. A. Lewis, K. Bertoldi, *Adv. Mater.* **2015**, *27*, 4296.
[47] E. Siéfert, E. Reyssat, J. Bico, B. Roman, *Nat. Mater.* **2019**, *18*, 24.
[48] A. Rafsanjani, L. Jin, B. Deng, K. Bertoldi, *Proc. Natl. Acad. Sci. USA* **2019**, *116*, 8200.
[49] W. Wu, W. Hu, G. Qian, H. Liao, X. Xu, F. Berto, *Mater. Des.* **2019**, *180*, 107950.
[50] L. Jin, A. E. Forte, B. Deng, A. Rafsanjani, K. Bertoldi, *Adv. Mater.* **2020**, *32*, 2001863.
[51] Y. Han, Z. Liu, S. Chen, J. Liu, Y. Wang, J. Li, *Photonics Research* **2020**, *8*, 1506.
[52] T. van Manen, S. Janbaz, M. Ganjian, A. A. Zadpoor, *Mater. Today* **2020**, *32*, 59.
[53] A. Robinson, A. Aziz, Q. Liu, Z. Suo, S. P. Lacour, *J. Appl. Phys.* **2014**, *115*, 14.
[54] O. H. Yeoh, *Rubber Chem. Technol.* **1993**, *66*, 754.

© 2021 Wiley-VCH GmbH